

# Low Potential Prussian Blue Analogs: Manganese Hexacyanochromate

Samuel Wheeler<sup>†</sup>, Isaac Capone<sup>†</sup>, Sarah Day<sup>‡</sup>, Chiu Tang<sup>‡</sup>, Mauro Pasta<sup>†,\*</sup>

<sup>†</sup> Department of Materials, University of Oxford, Parks Road, Oxford OX1 3PH, United Kingdom

<sup>‡</sup> I11 Beamline, Diamond Light Source Limited, Harwell Science and Innovation Campus, Chilton, Didcot OX11 0DE, United Kingdom.

**ABSTRACT:** Prussian blue analogues (PBAs) have recently shown outstanding electrochemical properties ascribable to their unique open-framework crystal structure that allows the reversible insertion of alkali ions with negligible perturbation to the framework itself. Many hexacyanoferrate materials have shown excellent properties and are some of the most promising sodium- and potassium-ion cathode materials in both aqueous and organic electrolytes. However, there is a distinct lack of candidate PBA materials that operate at low potentials as their characteristic crystalline framework shows instability. In this article we characterise the structure and electrochemical behavior of manganese hexacyanochromate which exhibits reversible sodium insertion at -0.86 V vs. SHE (1.84 V vs. Na<sup>+</sup>/Na), whilst maintaining the characteristic PBA cubic structure. This is the lowest redox potential of reported PBA materials and shows fast kinetics in a high voltage water-in-salt electrolyte. Further reduction in potential in an organic electrolyte shows decomposition of the crystalline structure

## INTRODUCTION

Prussian blue analogues (PBAs) are uniquely suitable as electrode materials for sodium ion (NIBs) and potassium ion batteries (KIBs) due to their open-framework structure, two possible redox centres, and compositional tunability<sup>1,2</sup>. Wide <100> ion conduction channels enable rapid solid-state diffusion of insertion ions. Large interstitial sites, larger than the insertion ion, and the robust framework result in minimal structural modification on ion insertion<sup>3</sup> (Figure 1a). They have been explored for many different applications because of their ease of synthesis and intriguing electrochemical and magnetic properties<sup>2</sup>.

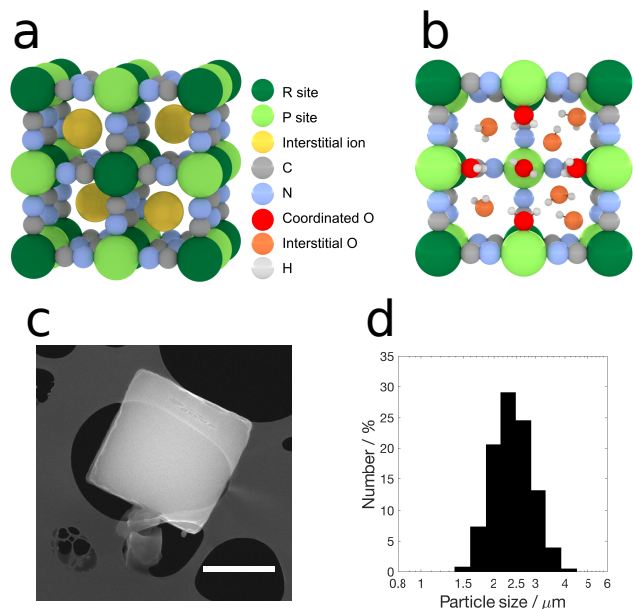


Figure 1: Schematic representation of cubic PBAs and morphology of MnHCCr. (a) the ‘ideal’ PBA crystal structure consisting of two distinct transition metal sites, P and R, denoted by light green and dark green spheres respectively. These transition metals are octahedrally coordinated to cyanide ligands forming the cubic structure. Grey and light blue spheres are carbon and nitrogen. Within the structure there are interstitial sites which can accommodate inserting ions, shown in yellow. (b) Hexacyanometalate vacancies,  $[\text{R}(\text{CN})_6]$ , are a major structural defect often up to 33% in PBA materials, and water is present in the

structure in two distinct bonding environments. (c) Scanning electron micrograph of as-synthesised MnHCCr, scale bar 1 μm. (d) Particle size distribution measured from dynamic light scattering (DLS) measurements.

Recently, we and others have utilized PBAs as battery materials with excellent cycle life and rate performance in both aqueous and organic electrolytes for NIBs and KIBs<sup>4-6</sup>. Most of the previous work has been dedicated to the electrochemistry of hexacyanoferrates, where the C-coordinated Fe reversibly varies its oxidation state between III and II at potentials around 0.8 V vs. SHE (3.5 V vs. Na<sup>+</sup>/Na), depending on the inductive effect of the N-coordinated transition metal ion, making them ideal positive electrode materials. The excellent properties of PBA cathode materials can only be fully exploited when combined in a full cell with an anode of comparable performance. This, and the lack of high performing sodium ion anode materials more generally, motivates the search for PBA compositions that operate at lower potentials.

We have previously shown how replacing the C-coordinated Fe with Mn lowers the insertion potential to about 0 V vs. SHE ( $\text{Mn}^{\text{II}}-\text{N}\equiv\text{C}-\text{Mn}^{\text{III/II}}$ ), approaching but within the thermodynamic stability limit of water<sup>7-9</sup>. Coupled with a copper hexacyanoferrate ( $\text{Cu}^{\text{II}}-\text{N}\equiv\text{C}-\text{Fe}^{\text{III/II}}$ ) cathode an aqueous full cell with high performance and an average discharge potential of 1 V was produced<sup>7</sup>. Manganese hexacyanomanganate also has a lower redox couple at -0.7 V vs. SHE ( $\text{Mn}^{\text{II}}-\text{N}\equiv\text{C}-\text{Mn}^{\text{II/I}}$ )<sup>8</sup>. A synthetic procedure to produce very low vacancy (1%) and water content MnHCMn was developed which produced the highest reported specific capacity of a PBA material of 209 mA h g<sup>-1</sup> over the three voltage plateaus. More recently the low potential redox couple of manganese hexacyanomanganate was used with high vacancy content (19%) material and operated in a water-acetonitrile co-solvent electrolyte giving an average full-cell voltage, with a copper hexacyanoferrate cathode, of 1.55 V<sup>9</sup>.

There have been efforts to develop PBA materials that have active redox couples at more negative potentials, however attempts to date have resulted in loss of the crystal structure and high reversible capacities ascribable to conversion-type mechanisms<sup>10-12</sup>. These works highlight issues that arise when

operating PBAs at low potentials in non-aqueous electrolytes but offer no explanation of the cause of structural breakdown.

By replacing the C-coordinated ion with Cr we can further reduce the redox potential<sup>13</sup>. In this work we characterise and investigate the redox behaviour of manganese hexacyanochromate ( $\text{Mn}^{\text{II}}\text{-N}\equiv\text{C-Cr}^{\text{III/II}}$ , referred to as MnHCCr in this paper) in a high voltage aqueous electrolyte. To the best of our knowledge, at - 0.86 V vs. SHE it has a lowest redox potential of all PBA compounds where the reversible ion insertion and structural integrity is confirmed. Further reduction in the potential within an organic electrolyte shows large irreversible capacity and a breakdown of the crystalline structure.

## EXPERIMENTAL

**Manganese hexacyanochromate synthesis.** 5 g of NaCN and 3 g of  $\text{CrCl}_3$  (excess  $\text{CrCl}_3$ ) were added to 120 ml of 0.1 M HCl solution. The solution was refluxed for 30 minutes. Then 4.819 g of 47.5%  $\text{Mn}(\text{NO}_3)_2$  solution was added under stirring in a dropwise manner. After 30 minutes the precipitate was centrifuged, washed three times with DI water and once with acetonitrile then dried overnight at 80°C in air.

**Manganese hexacyanoferrate synthesis.** 0.5 M  $\text{Na}_4\text{Fe}(\text{CN})_6$  solution was added in a dropwise manner to 1.5 M  $\text{Mn}(\text{NO}_3)_2$  solution under stirring at 30°C such that the final solution had a stoichiometric ratio of Fe to Mn. Both initial solutions contained 4 M NaCl. The solution was left to stir for 30 minutes then the precipitate was centrifuged, washed three times with DI water and once with acetonitrile then dried overnight at 80°C in air.

**Materials characterization.** Elemental composition was determined by inductively coupled plasma optical emission spectrometry (Perkin Elmer Optima 8000) and thermal analysis was performed using simultaneous thermogravimetric analysis mass spectrometry (NETZSCH STA 449 F3 Jupiter coupled to a QMS 403 Aëolos) under argon at a heating ramp of 5 °C per minute. Microscopy was carried out on a FE-SEM (Zeiss Merlin). Synchrotron X-ray diffraction was performed at beamline i11 at Diamond Light Source on the position sensitive detector (PSD). XRD of dehydrated MnHCCr samples and ex situ electrodes were performed inside a  $\text{N}_2$  filled glove box (Rigaku MiniFlex Cu source). Fourier transform infrared spectroscopy (Thermo Scientific Nicolet 6700) was performed in transmission mode using CsI pellets within a nitrogen filled glove box. Ex situ samples for XRD and FTIR were prepared by retrieving the carbon cloth electrodes, washing them with acetonitrile, then allowing them to dry before measurement. For FTIR samples the powder was then scraped from the carbon cloth. The General Structure Analysis System/Experiment Graphical User Interface (GSAS/EXPGUI) program was used for refinements<sup>14,15</sup>. The particle-size distribution was measured using dynamic light scattering (Malvern Zetasizer Nano ZS) using a He-Ne laser (633 nm). The sample was prepared by dispersing the powder in a 1:1 mixture of water/isopropanol through sonication.

**Electrochemical characterization.** Electrodes were prepared by mixing 80 wt% active material, 10 wt% carbon black (Timical SUPER C65) and 10 wt% polyvinylidene fluoride (PVDF, Kynar 2850 GL) in a mortar with 1-methyl-2-pyrrolidone to form a slurry. The slurry was pasted on carbon cloth (Fuel Cell

Earth AvCarb) with areal mass loadings of around 10  $\text{mg cm}^{-2}$ , then dried overnight at 80°C in air. Electrochemical measurements were performed on three electrode flooded cells inside an Ar filled glove box. The water-in-salt (WiS) electrolyte used was 37 m sodium bis(fluorosulfonyl)imide (NaFSI) in water (at the solubility limit). The organic electrolyte used was 1 M sodium perchlorate ( $\text{NaClO}_4$ ) in propylene carbonate (PC). For aqueous measurements the reference electrode was an Ag/AgCl pseudo reference prepared through oxidation of silver wire in HCl solution which was calibrated using a ferrocene internal standard. The counter electrode was MnHCFE. For non-aqueous measurements sodium metal was used as both reference and counter electrodes. Electrochemical measurements were performed on a BioLogic VMP3 potentiostat.

## RESULTS AND DISCUSSION

**Manganese hexacyanochromate: physio-chemical characterization.** MnHCCr was synthesised directly from  $\text{Mn}(\text{NO}_3)_2$ ,  $\text{CrCl}_3$  and NaCN in a one-pot two-step process (details in the **Experimental** section). The as-synthesised powder has large cubic particles (**Figure 1c**), with an average particle size of around 2.3  $\mu\text{m}$ . Inductively coupled plasma optical emission spectrometry (ICP-OES) and thermogravimetric analysis (TGA) were used to calculate chemical composition and water content respectively. The overall chemical formula was  $\text{Na}_{0.04}\text{Mn}[\text{Cr}(\text{CN})_6]_{0.70}\cdot 2.80\text{H}_2\text{O}$ . Manganese coordination environment is therefore approximately  $\text{MnN}_4\text{O}_2$ , the remaining water within a hydration shell around sodium ions and hydrogen bonded within interstitial sites.

Prussian blue analogues often crystallize in the cubic space group  $Fm\bar{3}m$ . The structure contains two distinct transition metal sites, R and P, which are in an FCC arrangement and bridged by cyanide ligands. MnHCCr takes this crystal structure, with Mn and Cr sitting at 4a and 4b sites respectively, whilst C and N taking 24e sites (x, 0, 0)<sup>16</sup>. Sodium sits at the centre of the interstitial site (8c). Water is present in the structure in two distinct bonding environments: co-ordinated water bonded directly to P-site transition metals within vacancies and zeolitic water which are distributed loosely-bound throughout the structure<sup>16,17</sup>.

High-resolution synchrotron powder diffraction data was taken of the hydrated MnHCCr which was used for structural refinement (**Figure 2**).

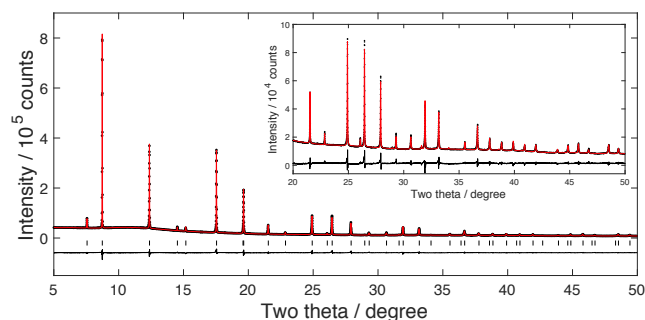


Figure 2: High-resolution synchrotron powder X-ray diffraction pattern of as-synthesised hydrated MnHCCr ( $\lambda = 0.824525 \text{ \AA}$ ).

Sodium was removed from the model due to its low occupancy, 0.04 per formula unit from ICP. Two oxygen sites were

included in the model, O(1) at 8c in the centre of the interstitial site and O(2) at 24e bonded to manganese in vacancies. In the model oxygen atoms represent water molecules, with hydrogen atoms removed due to their extremely low scattering. Similar treatment of water molecules in PBAs have been undertaken previously<sup>16,18,19</sup>. The occupancy values for Cr, C and N were restrained with respect to each other. Parameters refined were lattice parameter, site occupancies, fractional coordinates and atomic displacement parameters, as well as background, shift in x and peak shape function parameters. The model began with reasonable values for parameters and each additional parameter allowed to relax in turn until all parameters were being refined simultaneously. **Figure 2** shows the high-resolution XRD data with Rietveld fitting and residual. The large particle size and high crystallinity result in high-intensity well-defined peaks, even at high angles. Final refinement parameters are given in **Table 1**.

Atom	Site	g	x	y	z	$U_{iso}$
Mn	4a	1	0	0	0	0.02822(21)
Cr	4b	0.6931(6)	0.5	0	0	0.02259(30)
O(1)	8c	1.4218(29)	0.25	0.25	0.25	0.4025(16)
C	24e	0.6931(6)	0.30836(20)	0	0	0.0649(13)
N	24e	0.6931(6)	0.20041(15)	0	0	0.0344(8)
O(2)	24e	0.4124(18)	0.2449(4)	0	0	0.1908(18)

Table 1: Structural parameters of MnHCCr from Rietveld refinement in the space group  $Fm-3m$  ( $Z = 4$ ). Occupancy g, atomic positions (x, y, z), and isotropic atomic displacement  $U_{iso}$  are given. The lattice parameter is 10.803920(13) Å. Sodium is located at the centre of the interstitial A site whilst oxygen takes two positions, O(1) bonded to Mn in vacancies and O(2) at the centre of the interstitial site.  $R_p = 1.65\%$ ,  $R_{wp} = 2.79\%$ ,  $\chi^2 = 16.26$ , GOF = 4.03.

The lattice parameter is calculated to be 10.804 Å, within the range of previously reported values<sup>16,20,21</sup>. Lattice parameter is highly sensitive to level of hydration with accounts for the relatively wide range of values in literature. The hexacyanochromate vacancy content was calculated to be 31%, in good agreement with ICP results of 30%. The total water content within the refined model was higher than that calculated from TGA, 5.31 molecules per formula unit compared to 2.80 calculated from TGA. There are a few possible causes for this discrepancy including an overestimation in the value from the refined model, as electron density from sodium is being associated with oxygen, and an underestimation in the value from TGA, as the material is dehydrated prior to the measurement starting as the TGA chamber is evacuated and refilled. Supporting evidence that MnHCCr is dehydrated under vacuum is the lattice parameter difference between the hydrated MnHCCr synchrotron XRD refined lattice parameter of 10.804 Å to the laboratory XRD refined lattice parameter of 10.679 Å for hydrated MnHCCr being exposed to vacuum prior to measurement.

The two oxygen positions are reasonable and supported by TGA and FTIR data (**Figure 3**). The refinement gave an occupancy of 0.41 for O(2) coordinated water, close to the expected value of 0.3. High atomic displacement parameter for the zeolitic water, O(1), indicate that there are imperfections in the model. The high vacancy content and lack of apparent ordering of the

vacancies throughout the structure results in a number of local environments within the structure. In theory each interstitial site can be adjacent to zero, one, two, three or four hexacyanochromate vacancies. This in turn leads to a number of oxygen sites both at the centre of the interstitial site (8c) and displaced along the  $\langle 111 \rangle$  directions (32f) and  $\langle 110 \rangle$  directions (48g)<sup>18</sup>. Additionally, hydrogen bonding to coordinated water can result in lower energy positions off-centre<sup>16,17</sup>. This multitude of factors result in a particularly complex arrangement of water molecules within interstitial sites and efforts to further refine O(1) oxygen sites proved unsuccessful.

**Effect of water on structural stability.** Thermal analysis was performed through simultaneous thermal gravimetric analysis, differential scanning calorimetry and mass spectrometry, **Figure 3a**.

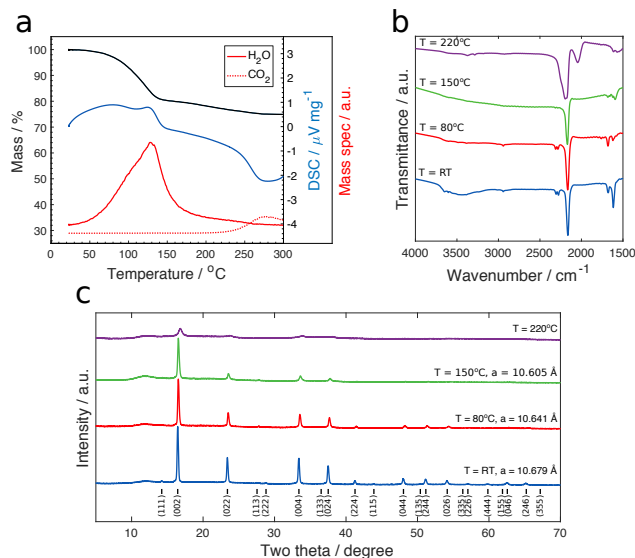


Figure 3: Dehydration of MnHCCr. The composition, bonding, and structure of MnHCCr was explored after heating at a series of temperatures. (a) The thermal gravimetric analysis (TGA) trace of as synthesised MnHCCr shows two distinct mass lost steps, the first accounting for 20% of initial mass, the second accounting for 5%. Simultaneous differential scanning calorimetry (DSC) shows distinct endothermic and exothermic processes. Mass spectrometry shows the first step is the dehydration of the material, followed by carbon dioxide evolution at higher temperature. (b) FTIR shows bonding within the samples. The stretching mode of CN, the most intense peak, is seen at 2164 cm<sup>-1</sup>. Different stretching and bending modes of water are responsible for absorption bands between 1600 – 1700 cm<sup>-1</sup> and 3100 – 3700 cm<sup>-1</sup>. (c) the dependence of structure on heating temperature is shown in XRD data.

Between 30°C and 150°C there is the first mass loss step, corresponding to dehydration of the materials as seen through the  $m/z=18$  mass spectrometry trace. Within this trace there are two distinct water evolutions steps which could correspond to water loss from two distinct environments, firstly the loosely bound zeolitic water and the second the coordinated water molecules at higher temperatures<sup>22</sup>. This is most clearly seen in the DSC trace as two distinguishable endothermic steps peaking at 80°C and 124°C. The second mass loss step shows CO<sub>2</sub> release which is indicative of breakdown of the crystalline structure.

In attempt to study the material at different levels of hydration samples were dried at RT, 80°C, 150°C and 220°C under

vacuum. The FTIR spectra and XRD patterns these samples are shown in **Figure 3b and c**. The characteristic stretching band of CN is the most intense peak and at  $2164\text{ cm}^{-1}$  in the most hydrated sample, increasing to  $2166\text{ cm}^{-1}$  then  $2170\text{ cm}^{-1}$  as water is removed. This is consistent with previous reports<sup>23</sup>. The broad band between  $3100\text{ cm}^{-1}$  and  $3700\text{ cm}^{-1}$  as well as the sharp peaks at  $3604\text{ cm}^{-1}$  and  $3650\text{ cm}^{-1}$  come from stretching modes of water in the sample. The strong broad peak corresponds to hydrogen bonded water molecules with rotational freedom. Heating to  $80^\circ\text{C}$  removes this absorption band. Sharp bands at  $3650\text{ cm}^{-1}$  and  $3604\text{ cm}^{-1}$  correspond to the symmetric and asymmetric stretching modes of coordinated water. Sharp absorption bands in the range  $1600 - 1700\text{ cm}^{-1}$  correspond to bending modes of water. In the hydrated sample two peaks are seen at  $1616\text{ cm}^{-1}$  and  $1678\text{ cm}^{-1}$ . On dehydration at  $80^\circ\text{C}$  the peak at  $1616\text{ cm}^{-1}$  reduces in intensity considerably whereas the peak at  $1678\text{ cm}^{-1}$  does not change. This leads to the conclusion that the less strongly bound zeolitic water is responsible for the peak at  $1616\text{ cm}^{-1}$  and coordinated water is responsible for the peak at  $1678\text{ cm}^{-1}$ <sup>124</sup>. Peaks in the IR spectra between  $2260\text{ cm}^{-1}$  and  $2320\text{ cm}^{-1}$  and at  $2945\text{ cm}^{-1}$  are from acetonitrile impurities introduced during the washing procedure.

XRD patterns of the same samples show a decrease in lattice parameter as the material is dehydrated and a loss in the crystalline structure at  $220^\circ\text{C}$ . Additionally, as the material is dehydrated the relative intensities of high angle reflections decrease considerably which is likely due to local structural distortion and increased microstrain. High-resolution synchrotron powder X-ray diffraction of MnHCCr dried at  $80^\circ\text{C}$  under vacuum is shown in **Supplementary Figure 1**. Refinement parameters in **Supplementary Table 1** show a larger decrease in interstitial water removal compared to coordinated water, further supporting the TGA-DSC-MS and FTIR data.

For electrochemical studies hydrated electrodes were used in the water-based electrolyte and electrodes dehydrated at  $150^\circ\text{C}$  under vacuum were used in a non-aqueous electrolyte. This dehydration temperature was chosen because much, if not all, of the water was removed but the crystalline structure was still present.

**Electrochemical characterization in a water-in-salt electrolyte.** The electrochemical behaviour of MnHCCr was characterised in a water-containing electrolyte. Experimentally it has been shown that PBAs exhibit extremely fast electrode kinetics in aqueous electrolytes, especially when the material has high vacancy content<sup>6,7</sup>. This is reportedly due to very low interfacial charge transfer and high ionic mobility within the structure as water shields local charges<sup>25</sup>. Additionally, DFT modelling has shown a stabilizing effect of structural water in PBA materials<sup>26</sup>. Since MnHCCr has such a low redox potential, much lower than the thermodynamic limit of water, the use of conventional aqueous electrolytes is prohibited.

In this study an aqueous ‘water-in-salt’ (WiS) sodium bis(fluorosulfonyl)imide (NaFSI) electrolyte at 37 m was used (prepared according to ref<sup>27</sup>). This is a new class of electrolytes for which the electrochemical stability window is significantly increased through reduced activity of water, strong bonding between water molecules and cations in solution, and potentially the formation of a  $\text{Na}^+$  conducting solid-electrolyte interphase<sup>27,28</sup>. This electrolyte was used as it has one of the widest

electrochemical stability windows of electrolytes that contain water.

The electrochemical stability window of this electrolyte was measured by LSV experiments on glassy carbon electrode at  $1\text{ mV s}^{-1}$  (**Figure 4a**).

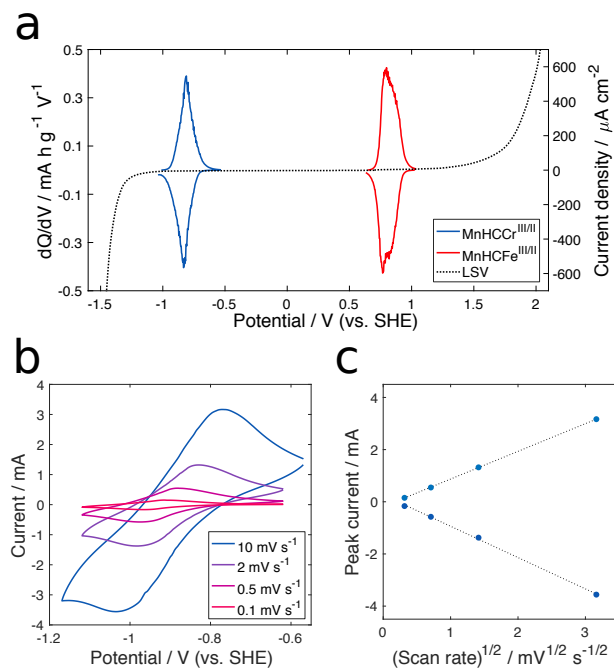


**Figure 4:** MnHCCr aqueous electrochemical characterisation. (a) linear sweep voltammetry (LSV) of the ‘water-in-salt’ (WiS) electrolyte was taken using a glassy carbon pin at  $1\text{ mV s}^{-1}$ , with the electrochemical stability limit defined as  $10\text{ }\mu\text{A cm}^{-2}$ . The  $dQ/dV$  of  $\text{Mn}^{\text{II}}-\text{N}=\text{C}-\text{Cr}^{\text{III/II}}$  and  $\text{Mn}^{\text{II}}-\text{N}=\text{C}-\text{Fe}^{\text{III/II}}$  are shown, centered at  $-0.86\text{ V vs. SHE}$  and  $0.80\text{ V vs. SHE}$  respectively. (b) cyclic voltammograms (CVs) of MnHCCr at scan rates from  $0.1 - 10\text{ mV s}^{-1}$ . (c) the peak current at each scan rate plotted against the square root of scan rate. The gradients of the lines of best fit are  $1.07\text{ mA mV}^{-1/2}\text{ s}^{1/2}$  and  $-1.20\text{ mA mV}^{-1/2}\text{ s}^{1/2}$ .

Using a current density limit of  $10\text{ }\mu\text{A cm}^{-2}$  the electrolyte has a lower stability limit of  $-1.07\text{ V vs. SHE}$  and a stability window of  $2.5\text{ V}$ . MnHCCr shows a reversible electrochemical reaction centred at  $-0.86\text{ V vs. SHE}$ , the  $dQ/dV$  of this reaction is shown in **Figure 4a** alongside  $\text{MnHCCr}^{\text{III/II}}$  for comparison. MnHCCr gave a reversible capacity of  $62\text{ mA h g}^{-1}$  which is expected from a single redox centre PBA material with vacancy content of 30%. A full PBA cell could be produced by coupling this with MnHCCr or any other PBA cathode material<sup>29</sup>.

Cyclic voltammograms at scan rates from  $0.1$  to  $10\text{ mV s}^{-1}$  were performed to study the redox reaction kinetics (**Figure 4b**). As the scan rate increases the peak separation increases and the peak current increases linearly with the root of scan rate. This behaviour is indicative of a one-electron one-step quasi reversible reaction within a diffusion limited regime.

For such systems the dependence of peak current,  $i_{\text{rate}}$  (mA), on scan rate is given by<sup>30</sup>

$$i_{\text{peak}} = 0.4463 \times \sqrt{\frac{n^3 F^3}{RT}} \times \sqrt{D} \times C_0 \times \sqrt{V_{\text{rate}}}$$



where  $n$  is the number of electrons involved in the reaction,  $D$  ( $\text{cm}^2 \text{s}^{-1}$ ) is the average diffusion coefficient,  $C_0$  ( $\text{mol cm}^{-3}$ ) is the concentration of active sites,  $V_{\text{rate}}$  ( $\text{mV s}^{-1}$ ) is the scan rate and  $F$ ,  $R$ , and  $T$  take their conventional meanings.  $C_0$  can be estimated from the specific capacity and density of the material. Using the gradient of the line of best fit during oxidation of  $1.07 \text{ mA mV}^{-1/2} \text{ s}^{1/2}$ , **Figure 4c**, gives an average diffusion coefficient of  $1.9 \times 10^{-6} \text{ cm}^2 \text{ s}^{-1}$ . This value is high for solid state diffusion and similar in order of magnitude to diffusion in other PBA compounds<sup>31</sup>.

To study the electrode reaction MnHCCr electrodes were cycled twice and then on the third discharge stopped at a series of charge states. Ex situ XRD patterns show that the structure remained cubic and **Figure 5a** shows the two-theta angle of the (024) peaks. The (024) peak is plotted to represent the change in lattice parameter as it is both of reasonably high intensity and at a high two-theta value, therefore giving large change in absolute angle as the lattice parameter contracts. Data over the full two-theta range is shown in **Supplementary Figure 2**.

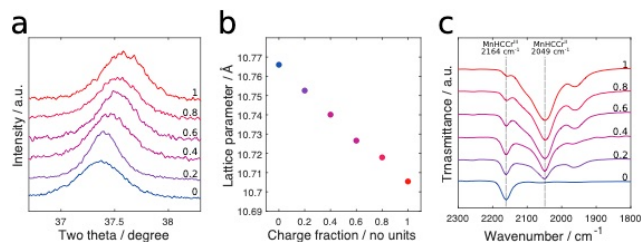


**Figure 5:** Ex-situ analysis of MnHCCr electrode reaction in an aqueous electrolyte at a series of charge states between 0 (oxidised) and 1.0 (reduced). Ex-situ XRD shows a linear contraction in the lattice on reduction, shown in (a) by the (024) diffraction peak moving to higher angles. The cubic structure of MnHCCr is maintained over the whole state of charge. In addition to the change in lattice parameter the intensity of the (022) and (004) peaks increased, compared to the (002), as the material is reduced, and sodium inserted, see **Supplementary Figure 2**. (b) shows the dependence of state of charge on lattice parameter, calculated through refinement of the lattice parameter of a cubic unit cell. Ex-situ FTIR was performed on the same electrodes and shows the change in  $\nu(\text{C}\equiv\text{N})$  absorption as the  $\text{CN}^-$  environment is changing. The absorption peak at  $2164 \text{ cm}^{-1}$  is characteristic of  $\text{Mn}^{\text{II}}-\text{C}\equiv\text{N}-\text{Cr}^{\text{III}}$  bonding whereas the peak at  $2049 \text{ cm}^{-1}$  is characteristic of  $\text{Mn}^{\text{II}}-\text{C}\equiv\text{N}-\text{Cr}^{\text{II}}$  bonding.

Refinement of the unit cell shows that the lattice parameter changes linearly with the state of charge over the whole range (**Figure 5b**). As the material is reduced, and sodium inserted into the material, the lattice parameter decreases. This peculiar behaviour is seen in other PBA materials and the change in lattice parameter is caused by the change in the  $\text{Cr}(\text{CN})_6^{n-}$  complex radius as it alters valence state<sup>32,33</sup>. The material exhibits a very low lattice parameter variation of  $\sim 0.6\%$  on cycling.

The position of the  $\nu(\text{C}\equiv\text{N})$  band is dependent on the bonding environment, and in the case of MnHCCr the oxidation state of Mn and Cr, which is analogous to other PBA materials<sup>7,18,34</sup>. Ex situ FTIR shows that as the material is reduced there is a decrease in the absorption peak at  $2164 \text{ cm}^{-1}$ , characteristic of  $\text{Mn}^{\text{II}}-\text{C}\equiv\text{N}-\text{Cr}^{\text{III}}$  bonding, and an increase in the peak at  $2049 \text{ cm}^{-1}$ , characteristic of  $\text{Mn}^{\text{II}}-\text{C}\equiv\text{N}-\text{Cr}^{\text{II}}$  bonding, **Figure 5c**. The FTIR spectrum over the full wavenumber range is presented in **Supplementary Figure 3**. Both the change in lattice parameter and FTIR spectra were observed to be fully reversible.

**Further reduction in potential in an organic electrolyte.** To explore the stability of the material at lower potentials the electrochemical behavior of the material was explored in an organic electrolyte (1 M  $\text{NaClO}_4$  in PC). The electrodes were dried under vacuum at  $150^\circ\text{C}$  to remove water within the structure before use. **Figure 6** shows the galvanostatic cycling performance, at  $15 \text{ mA g}^{-1}$ , of MnHCCr in WiS and in organic electrolyte with two different cut-off voltages. Additionally, ex situ XRD were taken at selected points. Operating in the organic electrolyte with the voltage cut-off at  $-1.3 \text{ V}$  MnHCCr shows the single reversible plateau corresponding to the reduction of chromium, as seen in the WiS electrolyte previously. Ex situ XRD confirms the structure is maintained. There is, however, lower capacity and slower kinetics when compared to performance in the WiS electrolyte. The  $\text{Na}^+$  diffusion coefficient of dehydrated MnHCCr was calculated to be  $3 \times 10^{-8} \text{ cm}^2 \text{ s}^{-1}$ , more than an order of magnitude lower than the hydrated material, see **Supplementary Figure 4**.

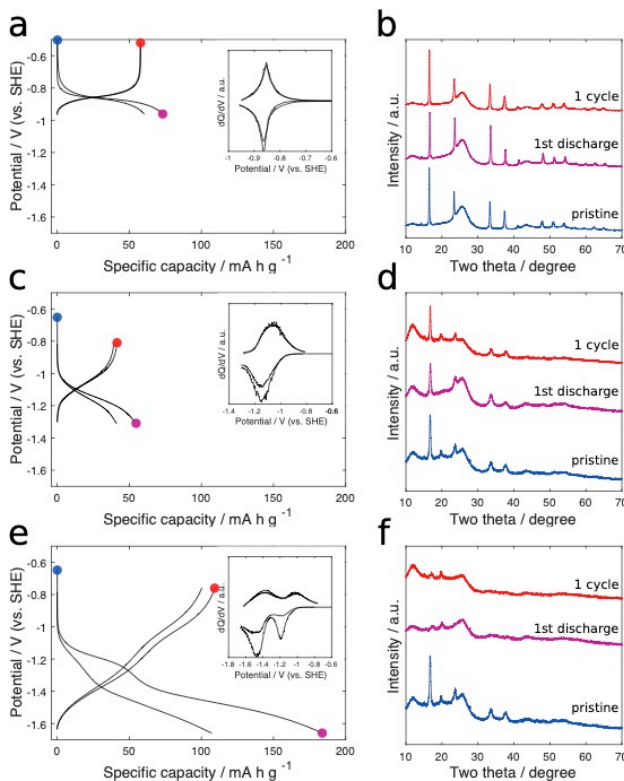


**Figure 6:** Behavior of MnHCCr during the first two cycles in the WiS electrolyte (a) and in an organic electrolyte with different voltage cut-offs (c and e). XRD patterns of ex situ samples are shown, taken in the pristine state, after one discharge and after one full discharge and charge cycle for each cycling conditions (b, d and f). Note samples cycled in the organic electrolyte were dried at  $150^\circ\text{C}$  under vacuum. Peaks in the XRD patterns at  $18.3^\circ$ ,  $19.8^\circ$  and  $27.8^\circ$  come from the PVDF binder, see **Supplementary Figure 5**.

With a cut-off voltage at  $-1.65 \text{ V}$  there is an additional voltage plateau centered at  $-1.45 \text{ V}$ . This plateau has a large irreversible capacity and corresponds to the permanent breakdown of the crystalline structure. This is a similar response to other PBA compositions that have been discharged to low potentials in non-aqueous electrolytes and where reversible capacity arises from conversion-type mechanisms<sup>10-12</sup>. Finding the limit of stability of the MnHCCr crystalline structure, and of PBA

compounds more generally, is significant and places fundamental limitations on the useable potential range of the material.

## CONCLUSIONS

In summary, we characterise the structure and electrochemical behavior of manganese hexacyanochromate which exhibits reversible sodium insertion at  $-0.86$  V vs. SHE, whilst maintaining the characteristic open-framework PBA structure. The material has a capacity of  $62 \text{ mA h g}^{-1}$  and a diffusion coefficient of  $1.9 \times 10^{-6} \text{ cm}^2 \text{ s}^{-1}$  whilst operating in a high voltage water-in-salt electrolyte. This capacity is a result of the one-electron reaction and the high hexacyanochromate vacancy content of 30% reducing the amount of redox active  $\text{Cr}^{\text{III/II}}$  sites. Ex situ XRD has shown that the materials exhibits very low strain, of less than 1%, on cycling.

MnHCCr has the lowest redox potential for which the preservation of the open-framework structure is confirmed, and charge storage is from sodium insertion and transition metal redox. This is important as the limit of stability of PBA materials at low potential is currently unknown. When investigating the material in an organic electrolyte the same redox couple is observed, and the diffusion coefficient was calculated to be more than an order of magnitude lower at  $3 \times 10^{-8} \text{ cm}^2 \text{ s}^{-1}$ . Reducing the potential lower than  $-1.3$  V vs. SHE resulted in irreversible loss in the crystal structure and a change in the charge storage mechanism.

This work deepens the understanding of the limits of stability of the materials system and the relationship between vacancy and water content to performance and stability. Further research should be focused on overcoming the partial solubility of PBA compounds in aqueous electrolytes that, currently, leads to poor cycle life.

## ASSOCIATED CONTENT

### Supporting Information

The Supporting Information is available free of charge on the ACS Publications website.

High-resolution synchrotron powder x-ray diffraction pattern, Reitveld refinement parameters and residual of MnHCCr dried under vacuum at  $80^\circ\text{C}$ , cyclic voltammograms and diffusion coefficient calculation of  $\text{Na}^+$  in dehydrated MnHCCr, PVDF binder x-ray diffractogram, and full two-theta range and wavenumber range of ex situ XRD and FTIR data of MnHCCr cycled in WiS electrolyte (PDF)

## AUTHOR INFORMATION

### Corresponding Author

\* Email: [mauro.pasta@materials.ox.ac.uk](mailto:mauro.pasta@materials.ox.ac.uk)

### Author Contributions

S.W. and M.P. designed electrochemical and physical measurements. S.W. and I.C., performed and analyzed electrochemical measurements and physical characterization. S.W., S.D., C.T. and M.P. designed and performed the synchrotron X-ray diffraction measurements. S.W. and M.P. wrote this paper.

### Notes

The authors declare no competing financial interests.

## ACKNOWLEDGMENT

We acknowledge Matteo Salamone whose preliminary work on this material system made a valuable contribution to paper. This publication arises from research funded by the John Fell Oxford University Press Research Fund. S.W. acknowledges financial support from EPSRC. We thank Diamond Light Source for access to beamline I11 (proposal number *EE14809-1*) that contributed to the results presented here.

## REFERENCES

- (1) Hurlbutt, K.; Wheeler, S.; Capone, I.; Pasta, M. Prussian Blue Analogs as Battery Materials. *Joule* **2018**, 2 (10), 1950–1960.
- (2) Qian, J.; Wu, C.; Cao, Y.; Ma, Z.; Huang, Y.; Ai, X. Prussian Blue Cathode Materials for Sodium-Ion Batteries and Other Ion Batteries. *Adv. Energy Mater.* **2018**, 1702619, 1–24.
- (3) Wessells, C. D.; Peddada, S. V.; Huggins, R. A.; Cui, Y. Nickel Hexacyanoferrate Nanoparticle Electrodes For Aqueous Sodium and Potassium Ion Batteries. *Nano Lett.* **2011**, 11, 5421–5425.
- (4) Pasta, M.; Wang, R. Y.; Ruffo, R.; Qiao, R.; Lee, H. W.; Shyam, B.; Guo, M.; Wang, Y.; Wray, L. A.; Yang, W.; et al. Manganese-Cobalt Hexacyanoferrate Cathodes for Sodium-Ion Batteries. *J. Mater. Chem. A* **2016**, 4 (11), 4211–4223.
- (5) Wang, L.; Song, J.; Qiao, R.; Wray, L. A.; Hossain, M. A.; Chuang, Y. De; Yang, W.; Lu, Y.; Evans, D.; Lee, J. J.; et al. Rhombohedral Prussian White as Cathode for Rechargeable Sodium-Ion Batteries. *J. Am. Chem. Soc.* **2015**, 137 (7), 2548–2554.
- (6) Wessells, C. D.; Huggins, R. a; Cui, Y. Copper Hexacyanoferrate Battery Electrodes with Long Cycle Life and High Power. *Nat. Commun.* **2011**, 2, 550.
- (7) Pasta, M.; Wessells, C. D.; Liu, N.; Nelson, J.; McDowell, M. T.; Huggins, R. A.; Toney, M. F.; Cui, Y. Full Open-Framework Batteries for Stationary Energy Storage. *Nat. Commun.* **2014**, 5, 3007.
- (8) Lee, H.-W.; Wang, R. Y.; Pasta, M.; Woo Lee, S.; Liu, N.; Cui, Y. Manganese Hexacyanomanganate Open Framework as a High-Capacity Positive Electrode Material for Sodium-Ion Batteries. *Nat. Commun.* **2014**, 5, 5280.
- (9) Firouzi, A.; Qiao, R.; Motallebi, S.; Valencia, C. W.; Israel, H. S.; Fujimoto, M.; Wray, L. A.; Chuang, Y. De; Yang, W.; Wessells, C. D. Monovalent Manganese Based Anodes and Co-Solvent Electrolyte for Stable Low-Cost High-Rate Sodium-Ion Batteries. *Nat. Commun.* **2018**, 9, 861.
- (10) Deng, L.; Yang, Z.; Tan, L.; Zeng, L.; Zhu, Y.; Guo, L. Investigation of the Prussian Blue Analog  $\text{Co}_3[\text{Co}(\text{CN})_6]_2$  as an Anode Material for Nonaqueous Potassium-Ion Batteries. *Adv. Mater.* **2018**, 1802510.
- (11) Nie, P.; Shen, L.; Luo, H.; Ding, B.; Xu, G.; Wang, J.; Zhang, X. Prussian Blue Analogues: A New Class of Anode Materials for Lithium Ion Batteries. *J. Mater.*

- (12) Shibata, T.; Takachi, M.; Moritomo, Y. Low Voltage Charge/Discharge Behavior of Manganese Hexacyanoferrate. *Batteries* **2017**, 3 (1), 7.
- (13) Scholz, F.; Dostal, A. The Formal Potentials of Solid Metal Hexacyanometalates. *Angew. Chemie Int. Ed. English* **1995**, 34 (2324), 2685–2687.
- (14) Von Dreele, R. B.; Larson, A. C. General Structure Analysis Sytem (GSAS). *Los Alamos Natl. Lab LAUR*, 86–748.
- (15) Toby, B. H. EXPGUI a Graphical User Interface for GSAS. *J. Appl. Cryst* **2001**, 34, 210–213.
- (16) Güdel, H. U.; Stucki, H.; Ludi, A. The Crystal Structure of Manganese(II) Hexacyanochromate(III),  $\text{Mn}_3[\text{Cr}(\text{CN})_6]_2 \cdot x\text{H}_2\text{O}$ . *Inorganica Chim. Acta* **1973**, 7, 121–124.
- (17) Herren, F.; Ludi, A.; Fischer, P.; Halg, W. Neutron Diffraction Study of Prussian Blue,  $\text{Fe}_4[\text{Fe}(\text{CN})_6]_3 \cdot x\text{H}_2\text{O}$ . Location of Water Molecules and Long-Range Magnetic Order. *Inorg. Chem.* **1980**, 19 (4), 956–959.
- (18) Ojwang, D. O.; Grins, J.; Wardecki, D.; Valvo, M.; Renman, V.; Häggström, L.; Ericsson, T.; Gustafsson, T.; Mahmoud, A.; Hermann, R. P.; et al. Structure Characterization and Properties of K-Containing Copper Hexacyanoferrate. *Inorg. Chem.* **2016**, 55 (12), 5924–5934.
- (19) Wang, R. Y.; Shyam, B.; Stone, K. H.; Weker, J. N.; Pasta, M.; Lee, H. W.; Toney, M. F.; Cui, Y. Reversible Multivalent (Monovalent, Divalent, Trivalent) Ion Insertion in Open Framework Materials. *Adv. Energy Mater.* **2015**, 5 (12), 1–10.
- (20) Dong, W.; Zhu, L. N.; Song, H. Bin; Liao, D. Z.; Jiang, Z. H.; Yan, S. P.; Cheng, P.; Gao, S. A Prussian-Blue Type Ferrimagnet  $\text{Na}[\text{MnCr}(\text{CN})_6]$ : Single Crystal Structure and Magnetic Properties. *Inorg. Chem.* **2004**, 43 (8), 2465–2467.
- (21) Ferrari, A.; Tani, M. E.; Morisi, E. The Crystal Structure of Hexacyanochromate(III) of Divalent Cations. *Acta Crystallogr.* **1962**, 15 (1), 90–90.
- (22) Åkerblom, I. E.; Ojwang, D. O.; Grins, J.; Svensson, G. A Thermogravimetric Study of Thermal Dehydration of Copper Hexacyanoferrate by Means of Model-Free Kinetic Analysis. *J. Therm. Anal. Calorim.* **2017**, 129 (2), 721–731.
- (23) Brown, D. B.; Shriver, D. F. Structures and Solid-State Reactions of Prussian Blue Analogs Containing Chromium, Manganese, Iron, and Cobalt. *Inorg. Chem.* **1969**, 8 (1), 37–42.
- (24) Avila, M.; Reguera, L.; Rodríguez-Hernández, J.; Balmaseda, J.; Reguera, E. Porous Framework of  $\text{T}_2[\text{Fe}(\text{CN})_6] \cdot x\text{H}_2\text{O}$  with T=Co, Ni, Cu, Zn, and H<sub>2</sub> Storage. *J. Solid State Chem.* **2008**, 181 (11), 2899–2907.
- (25) Mizuno, Y.; Okubo, M.; Hosono, E.; Kudo, T.; Zhou, H.; Oh-Ishi, K. Suppressed Activation Energy for Interfacial Charge Transfer of a Prussian Blue Analog Thin Film Electrode with Hydrated Ions ( $\text{Li}^+$ ,  $\text{Na}^+$ , and  $\text{Mg}^{2+}$ ). *J. Phys. Chem. C* **2013**, 117 (21), 10877–10882.
- (26) Xiao, P.; Song, J.; Wang, L.; Goodenough, J. B.; Henkelman, G. Theoretical Study of the Structural Evolution of a  $\text{Na}_2\text{FeMn}(\text{CN})_6$  Cathode upon Na Intercalation. *Chem. Mater.* **2015**, 27 (10), 3763–3768.
- (27) Kühnel, R.-S.; Reber, D.; Battaglia, C. A High-Voltage Aqueous Electrolyte for Sodium-Ion Batteries. *ACS Energy Lett.* **2017**, 2, 2005–2006.
- (28) Suo, L.; Borodin, O.; Wang, Y.; Rong, X.; Sun, W.; Fan, X.; Xu, S.; Schroeder, M. A.; Cresce, A. V.; Wang, F.; et al. “Water-in-Salt” Electrolyte Makes Aqueous Sodium-Ion Battery Safe, Green, and Long-Lasting. *Adv. Energy Mater.* **2017**, 7 (21), 1–10.
- (29) Nakamoto, K.; Sakamoto, R.; Sawada, Y.; Ito, M.; Okada, S. Over 2 V Aqueous Sodium-Ion Battery with Prussian Blue-Type Electrodes. *Small Methods* **2018**, 1800220.
- (30) Bard, A. J.; Faulkner, L. R. *Electrochemical Methods: Fundamentals and Applications*, John Wiley, New York, 2<sup>nd</sup> edn, 1980.
- (31) Lee, H.-W.; Pasta, M.; Wang, R. Y.; Ruffo, R.; Cui, Y. Effect of the Alkali Insertion Ion on the Electrochemical Properties of Nickel Hexacyanoferrate Electrodes. *Faraday Discuss.* **2014**, 176, 69–81.
- (32) Deeth, R. J. A Theoretical Rationale for the Formation, Structure and Spin State of Pentacyanochromate(II). *Eur. J. Inorg. Chem.* **2006**, 13, 2551–2555.
- (33) Takachi, M.; Matsuda, T.; Moritomo, Y. Cobalt Hexacyanoferrate as Cathode Material for  $\text{Na}^+$  Secondary Battery. *Appl. Phys. Express* **2013**, 6 (2).
- (34) Gerber, S. J.; Erasmus, E. Electronic Effects of Metal Hexacyanoferrates: An XPS and FTIR Study. *Mater. Chem. Phys.* **2018**, 203, 73–81.

